Supplementary Information

Selective Synthesis of Dense High-Spin *D*1 Active Sites via Engineered Less-Graphitized Carbon Environments

Xuan Luo[1], Jia-Bao Nie[1], Huang Liang[1], Yu-Yang Li[2], You-Heng Wang[1], Qi-Kang Que[3], Jean-Pol Dodelet[4]* and Yu-Cheng Wang[1,3]*

[1]State Key Laboratory of Physical Chemistry of Solid Surfaces, College of Chemistry and Chemical Engineering, Xiamen University, Xiamen 361005, China.

[2]GRINM (Guangdong) Institute for Advanced Materials and Technology,Foshan 528000, China.

[3]Innovation Laboratory for Sciences and Technologies of Energy Materials of Fujian Province (IKKEM), Xiamen 361005, China.

[4]INRS-Énergie, Matériaux et Télécommunications, Varennes, Quebec J3X1P7, Canada.

*Corresponding author. Email: Jean-Pol.Dodelet@inrs.ca, wangyc@xmu.edu.cn

Experimental Section

Materials

Zinc nitrate hexahydrate [$Zn(NO_3)_2 \cdot 6H_2O$, analytical reagent, AR, ≥99.0 %], 2-methylimidazole (2-mIm, ≥98 %), Ascorbic acid ($C_6H_8O_6$, AR, 99.7 %), Sulfuric acid (H_2SO_4, 95.0~98.0%), ferric chloride hexahydrate ($FeCl_3 \cdot 6H_2O$, 99.0%), Hydrochloric acid (HCl, 37%), Methanol (AR), Ethanol (AR), Isopropyl alcohol (AR), Sodium nitrite ($NaNO_2$, AR, 99%) and sodium acetate (CH_3COONa, AR, 99%) were purchased from Sinopharm. Pt/C catalyst (60 wt.%) and Proton exchange membrane pretreatment (NR 211) were purchased from Yangzhou Xingqiao Energy Co., Ltd. Gas diffusion layer (Ballard G3260) and gas diffusion layer (Toray TGP-H-060) were purchased from Suzhou Sinero Technology Co., Ltd., ^{57}Fe foil was purchased from Dalian Institute of Chemical Physics, Chinese Academy of Sciences. Nafion (D520, 5%, Dupont), Deionized water (Homemade, 18 megohms). All the above reagents are ready to use in their analytical purity and do not require reprocessing. $^{57}FeCl_3$ were obtained by dissolving ^{57}Fe foil in HCl solutions (1M, excess in volume) with oxidation by H_2O_2.

Catalyst preparation

Preparation of ZIF-8 precursor. The synthesis process unfolds as follows: Initially, dissolve 13.575g of 2-mIm and 12.6g of $Zn(NO_3)_2 \cdot 6H_2O$ separately in 450 mL of methanol, employing sonication until fully dissolved. Combine the two solutions to a total of 900 mL and subject the mixture to an additional 10 minutes of sonication. After sonication, let the mixture stand at ambient temperature, sealed with cling film, for 10-12 hours to allow ZIF dispersion formation. Following this period, centrifuge the resultant product and wash it three to four times with methanol. Dry the product at 80°C for a minimum of 3 hours, yielding over 2g of ZIF-8 precursor.

Fe-doping in ZIF-8 precursor. The preparation commenced with dissolving 20 mg of $FeCl_3 \cdot 6H_2O$ in 5 mL of methanol, to which 52 mg of AA was added, followed by sonication until a clear, colorless Fe-AA solution was achieved. Concurrently, 400 mg of ZIF-8 precursor was blended with 75 mL of anhydrous methanol and sonicated to create a white, milky dispersion. Subsequently, the Fe-AA solution was incrementally introduced to the ZIF-8 suspension, resulting in a purple coloration upon integration. The combined mixture was then stirred magnetically at 800 rpm for a duration of 10 hours. Post-stirring, the solution was centrifuged with methanol to yield a clear supernatant, followed by drying at 80°C for 5 hours, culminating in the synthesis of Fe-ZIF-AA. Fe-ZIF was prepared using the same procedure, except for the exclusion of AA. The reference sample (Fe-ZIF) without the addition of AA was prepared via a similar protocol.

Pyrolysis of Fe-ZIF-AA or Fe-ZIF precursors. The Fe-ZIF-AA or Fe-ZIF precursor underwent pyrolysis under an argon shield at 1000°C to synthesize the Fe/N/C-AA or Fe/N/C catalyst. Temperature elevation from room level to 1000°C occurred at a gradient of 5°C per minute, sustaining the peak temperature for an hour before cooling naturally to ambient conditions. This process produced a black powder, which was then meticulously pulverized using a mortar and pestle. The refined powder was preserved in a vial under argon to safeguard against contamination, readying it for further application.

Preparation of catalyst inks and working electrode

Preparation of Fe-N-C WE. To prepare the Fe-N-C catalysts ink, 6 mg of the catalyst was combined with 500 μL DI water and 450 μL ethanol, followed by 45 minutes of sonication to ensure homogenous dispersion. Subsequently, 50 μL of a 5 wt.% Nafion solution was introduced into the mix, with sonication continued for an additional 40 minutes to achieve a uniformly dispersed catalyst ink. Then, 25 μL of this ink was uniformly deposited onto an electrode surface measuring 0.2475 cm^2 and dried under an infrared lamp, forming a thin-film electrode. This process resulted in a catalyst loading of 0.6 mg cm^{-2}, with Nafion constituting 28% of the total dry weight.

ORR polarization curves testing

For the electrochemical tests, a homemade electrolytic cell is used with a carbon rod and saturated calomel electrode as counter and reference electrodes, respectively. The electrochemical workstation used is the CHI760E, which is coupled with a PINE rotating ringdisk device. RDE and RRDE tests are performed using this setup. Into the electrolytic cell, 0.1 M H_2SO_4 electrolyte was introduced, followed by O_2 bubbling to establish an O_2-rich atmosphere. The electrode was set 1-2 cm above the capillary, with activity assessments conducted at 900 rpm and applying 80% solution resistance compensation throughout the tests. The CV was subsequently measured under Ar-saturated conditions using identical parameters as the background measurement. The scan rate was set at 10 mV s^{-1} with a potential window of 0.2-1.0 V_{RHE}. The polarization curve was obtained by subtracting the Ar-background from the O_2-saturated CV curve, followed by averaging the forward and reverse scan curves.

Nitrite stripping experiments

The Fe/N/C catalyst containing exposed Fe particles must be pre-processed with acid washing to remove the exposed Fe particles. The acid washing procedure involves using 20 mg of the catalyst with 100 mL of 0.5 M H_2SO_4, followed by ultrasonic treatment for 1 hour, soaking at room temperature for 12 hours, repeated centrifuge washing, and vacuum drying at 70°C. Configure the Ink according to the ORR polarization curve testing process, applying 0.27 mg cm^{-2} of catalyst. The testing procedure is as follows: Sweep from -0.2 to 1.0 V_{RHE} in O_2-saturated 0.5 M sodium acetate solution (pH=5.2) at a sweep rate of 100 mV s^{-1} for at least 10 cycles until stability is achieved; then, test in Ar-saturated 0.5 M sodium acetate solution (pH=5.2) at -0.3 to -0.4 V_{RHE}, 1600 rpm, with a sweep rate of 10 mV s^{-1}, to obtain the background signal. Poisoning process: Maintain open circuit, immerse the working electrode in 0.125 M $NaNO_2$ solution for 5 minutes at 300 rpm; maintain open circuit, immerse the working electrode in deionized water for 1 minute at 300 rpm; maintain open circuit, immerse the working electrode in sodium acetate solution (pH=5.2) for 5 minutes at 300 rpm; maintain open circuit, immerse the working electrode in deionized water for 1 minute at 300 rpm. After the poisoning, test the CV curve: Sweep from -0.3 to -0.4 V_{RHE}, 1600 rpm, at a sweep rate of 10 mV s^{-1} in Ar-saturated 0.5 M sodium acetate solution (pH=5.2). The mass-normalized reduction charge (Q, C g^{-1}) of pre-adsorbed N-oxide was integrated in the range of -0.2 to 0.2 V_{RHE} by subtracting background current. The ASD was then calculated by the following formula of ASD (μmol sites g^{-1}) = Q / (n*F), where n represents the number of electrons transferred (n = 5), and F is the Faraday constant (96,485 C mol^{-1}).

Fuel cell testing

MEA preparation and single cell assembly. The Fe/N/C-AA catalyst, weighing 22 mg, was combined with 1.6 mL isopropanol and 0.4 mL deionized water, followed by an hour of ultrasonic dispersion in an ice bath. Subsequently, 352 mg of 5 wt.% Nafion solution was introduced, with an additional hour of ultrasonic dispersion to formulate the catalyst ink. This ink was then drop-cast onto a 2.5×2.5 cm^2 GDL and dried at 80°C to facilitate solvent evaporation, yielding a GDE with a catalyst density of 3.5 mg cm^{-2} and Nafion contributing 44% of the total dry weight. The GDE was trimmed to a precise 2.3×2.3 cm^2. For MEA assembly, this cathode was paired with a commercial Pt/C anode GDE, featuring 0.4 mg cm^{-2} Pt loading and a Nafion 211 membrane, and hot-pressed at 130°C at 7 MPa pressure for 120s. Gasket thicknesses of 125 μm and 175 μm were utilized on the anode and cathode sides, respectively. The completed MEA was then installed in a single cell setup, incorporating bipolar plates and heating plates on both sides. A control MEA, employing a Pt/C cathode with 0.1 mg cm^{-2} Pt loading, underwent a similar preparation and assembly process for comparative analysis.

H_2-air polarization curves testing. The single cell operation was conducted using a RCHE-1000 fuel cell test system (Voltammetry Hydrogen Energy Scientific Co., Ltd, Xiamen), setting H_2 (99.999%) and air (99.999%) flow rates at 0.7 L mn^{-1} and 1.7 L min^{-1}, respectively, with back pressure options of 0.5 or 1.0 bar, and maintaining a cell temperature of 80°C. Both cathode and anode gases were humidified to 100% RH. After stabilizing the OCV for 10 minutes under H_2-air atmosphere, data acquisition in constant voltage mode began. Measurements were taken at 25 mV intervals from OCV to 0.7 V, and at 50 mV intervals from 0.7 V down to 0.2 V. Each voltage point was maintained for 45 seconds, recording the average current during the last 15 seconds as the measurement current. This process was repeated, and the means of the two sets of polarization curves were calculated to derive the final data.

H_2-air fuel cell stability testing. The single cell operation was conducted using a RCHE-1000 fuel cell test system (Voltammetry Hydrogen Energy Scientific Co., Ltd, Xiamen). The testing mode involved a constant voltage stability test, where, following the polarization curve assessment, the cell voltage was held at 0.6 V for the duration testing. The test conditions for stability testing are as follows: H_2 (99.999%) flow rate at 0.7 L min^{-1}, air flow rate at 1.7 L min^{-1}, back pressure at 1 bar, cell temperature at 80°C, 100% RH for both cathode and anode gases. After stabilizing the OCV for 10 minutes under H_2-air atmosphere, measurements were taken in constant voltage mode, the constant voltage treatment was executed for 60 hours under 0.6 V.

H_2-O_2 polarization curves testing. The single cell operation was conducted using a RCHE-1000 fuel cell test system (Voltammetry Hydrogen Energy Scientific Co., Ltd, Xiamen), setting H_2 (99.999%) and O_2 (99.999%) flow rates at 0.7 L mn^{-1} and 0.35 L min^{-1}, respectively, with back pressure of 0.5 bar, and maintaining a cell temperature of 80°C. Both cathode and anode gases were humidified to 100% RH. After stabilizing the OCV for 10 minutes under H_2-O_2 atmosphere, data acquisition in constant voltage mode began. Measurements were taken at 25 mV intervals from OCV to 0.6 V. Each voltage point was maintained for 45 seconds, recording the average current during the last 15 seconds as the measurement current.

Characterizations

XRD were obtained from X-ray Powder Diffractometer (Rigaku Ultima-IV), The tube voltage was set to 35 kV, and the tube current was 15 mA. The measurement angle range was from 5° to 90°, with a scanning speed of 10°/min. XAS measurements were performed at the Beijing Synchrotron Radiation Facility (BSRF) line station 1W1B. All tests were performed in fluorescence mode with a fast scan of iron from 250 eV below the K-edge (7112 eV) to 550 eV above the K-edge. Data reduction, data analysis and were performed with the Athena software packages. Soft XAS was performed in National Synchrotron Radiation Laboratory (NSRL). The Mossbauer spectra were obtained at room temperature on a WISSEL WSS-10 Mossbauer Spectroscopy, with a ^{57}Co/Rh ray source and a homogeneous shift calibrated by the spectrum of α-Fe at room temperature. All Mössbauer spectral parameters of molecules and Fe/N/Cs were determined based on spectra obtained at room temperature. Additionally, low-temperature Mössbauer spectra were utilized to detect the Fe particles (such as Fe oxides, magnetic Fe and Fe carbide) in the Fe/N/Cs. The spectra were analyzed using the MossWinn program, and the exact parameters required were obtained by least-squares fitting of Lorentzian lines and related parameters. HAADF-STEM and elemental mapping were obtained from Spherical aberration corrected transmission electron microscope (AC-TEM, JEOL JEM-ARM300F2). Transmission electron microscope images were obtained from transmission electron microscope (JEOL JEM-2100). The metal content of the samples was determined by the ICP-OES (SPECTROBLUE FMX36). Scanning electron microscope (SEM) images were acquired on Zeiss Sigma 300. Raman spectra were performed using the Confocal micro-Raman spectrometer (HORIBA Xplo-RA). The isothermal adsorption/desorption and pore size distribution were obtained from automatic specific surface area and pore size analyzer (JWGB JW-BK100).

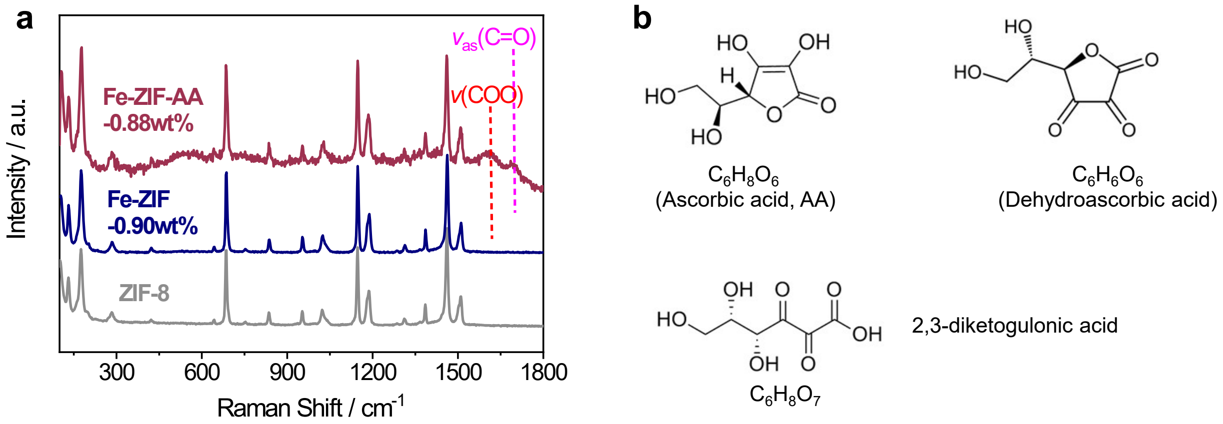

Fig. S1. (a) Raman spectra of Fe-ZIF-AA, Fe-ZIF and ZIF precursor. (b) The molecular structures and formulas for ascorbic acid, dehydroascorbic acid, and 2,3-diketogulonic acid.

Compared to Fe-ZIF and ZIF, Fe-ZIF-AA exhibited vibrational peaks of C=O and COO^-. These signals originate from the oxidation product of AA, 2,3-diketogulonic acid. During the doping process, AA was oxidized by Fe^{3+} and O_2, producing 2,3-diketogulonic acid and H_2O_2. The reaction equation is as follows:

$$\mathrm{Fe(III)^{**}} + C_6H_8O_6 + O_2 \rightarrow \mathrm{Fe(III)^{**}} + C_6H_6O_6 + H_2O_2$$

$$C_6H_6O_6 + H_2O \rightarrow C_6H_8O_7$$

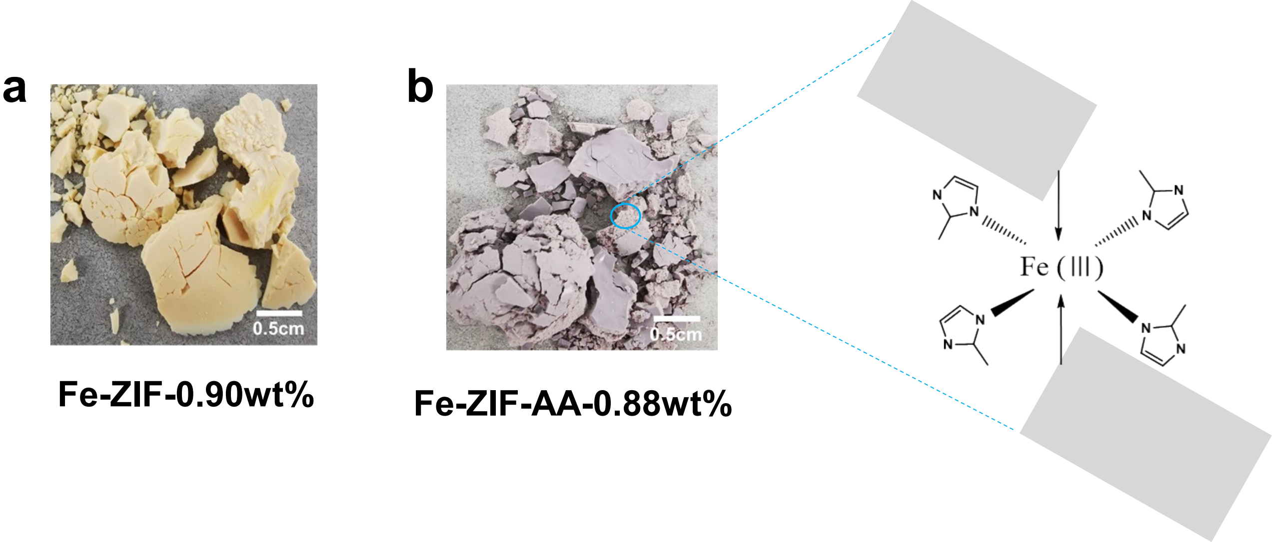

Fe-ZIF-0.90wt%

Fe-ZIF-AA-0.88wt%

Fig. S2. (a) Color of Fe-ZIF-0.90wt%. (b) Color of Fe-ZIF-AA-0.88wt%. The right figure shows the coordination configuration of Fe (III) after the introduction of AA.

Fe-ZIF appears yellow, whereas Fe-ZIF-AA displays a distinct purple hue. This color difference likely arises from a change in the coordination environment of Fe (III) upon the introduction of AA. In the modified structure, Fe (III) is coordinated by four imidazole ligands and two 2,3-diketogulonic acid molecules.

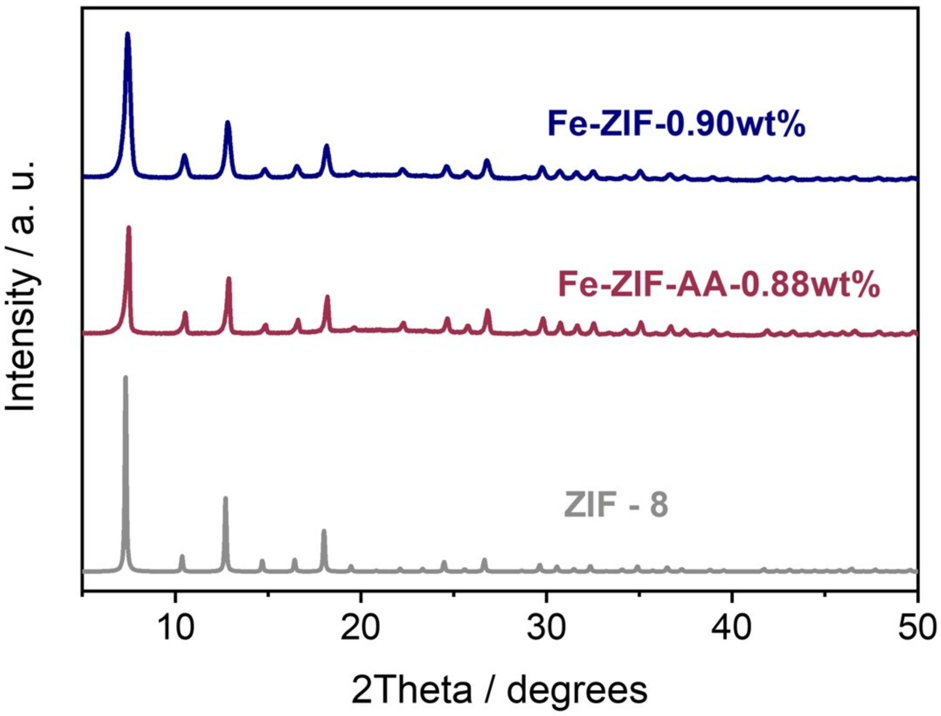

Fig. S3. XRD patterns of Fe-ZIF and Fe-ZIF-AA precursors. ZIF simulated pattern was also shown for comparison.

The addition of AA does not alter the diffraction patterns of ZIF-8, indicating that the framework structure of ZIF remains unchanged.

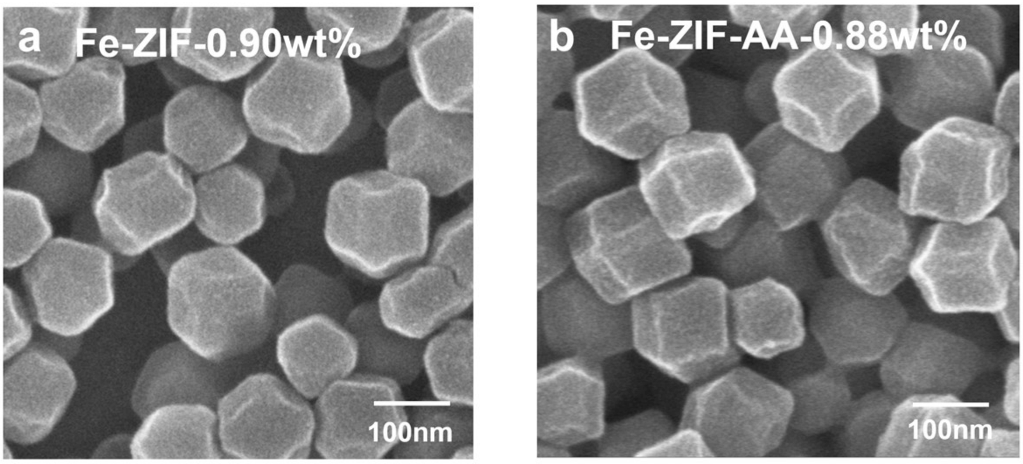

Fig. S4. SEM images of (a) Fe-ZIF-0.90wt% and (b) Fe-ZIF-AA-0.88wt%.

The SEM images of the two samples both exhibit a uniform polyhedral structure, with no noticeable differences observed.

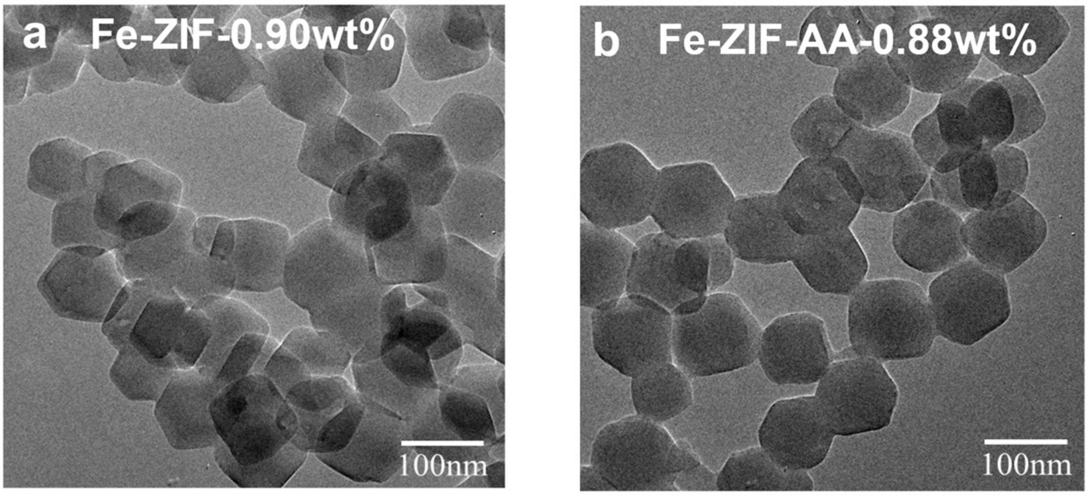

Fig. S5. TEM images of (a) Fe-ZIF-0.90wt% and (b) Fe-ZIF-AA-0.88wt%.

TEM images of Fe-ZIF-0.9wt% and Fe-ZIF-AA-0.88wt% show similar ZIF-8 structures, suggesting that AA does not alter the structural integrity of the ZIF-8 precursor.

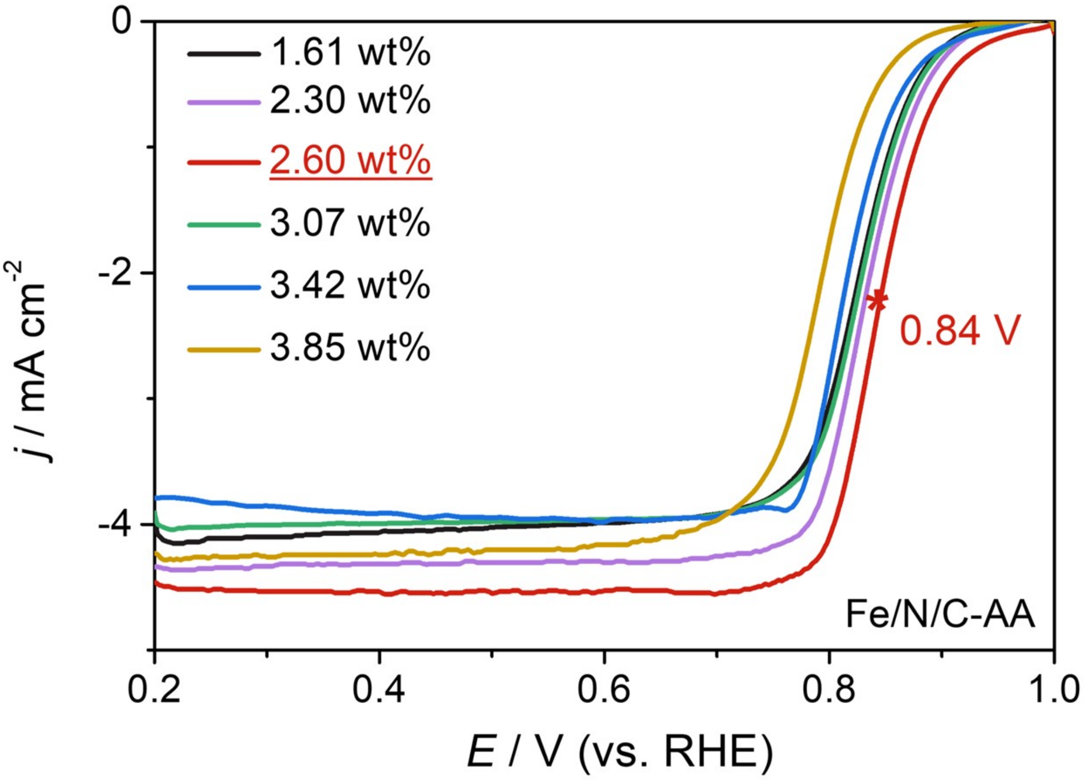

Fig. S6. The ORR activity of Fe/N/C-AA with different Fe content.

Among the six catalysts, Fe/N/C-AA-2.60wt% exhibits the highest ORR activity, as evidenced by a half-wave potential of 0.84 V. This suggests that a 2.60wt% Fe content is optimal.

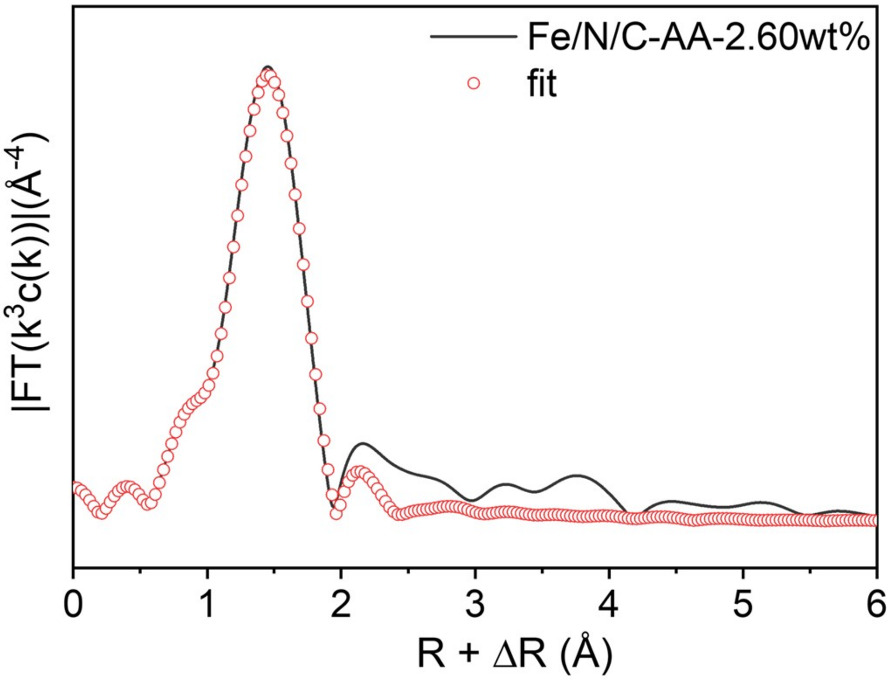

Fig. S7. FT-EXAFS of the Fe/N/C-AA-2.60wt%. The fitting parameters are presented in Table S1.

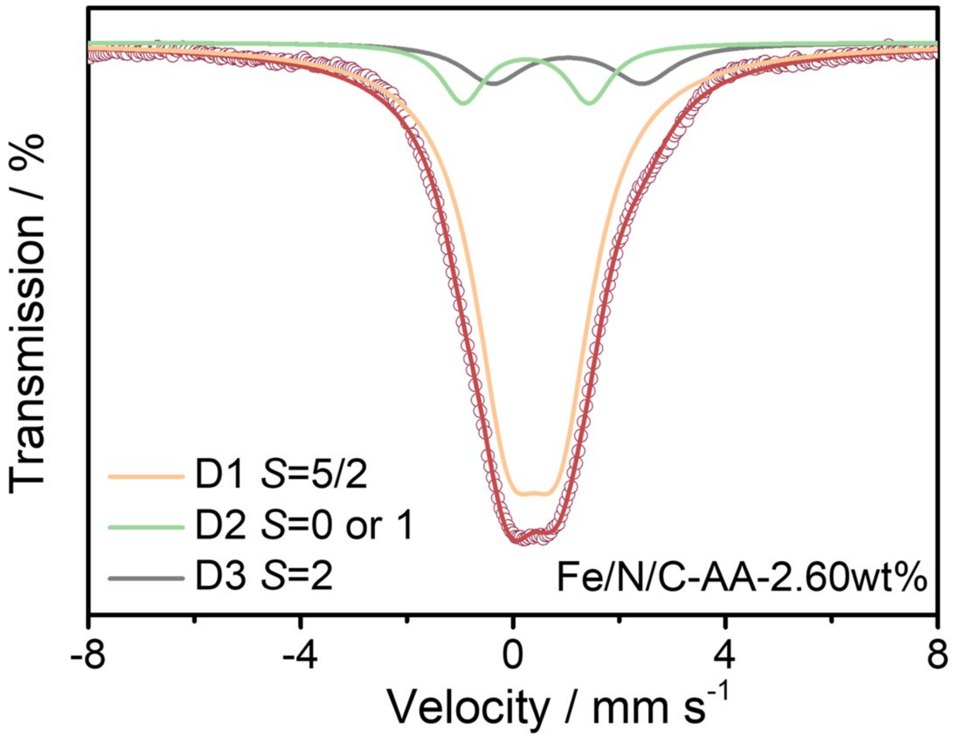

Fig. S8. Low-temperature (77K) Mössbauer spectroscopy of Fe/N/C-AA-2.60wt%.

Low-temperature Mössbauer spectroscopy did not detect any signals associated with aggregated states of Fe. This result indicates that the Fe sites of the Fe/N/C-AA catalyst exist in a single-atom state.

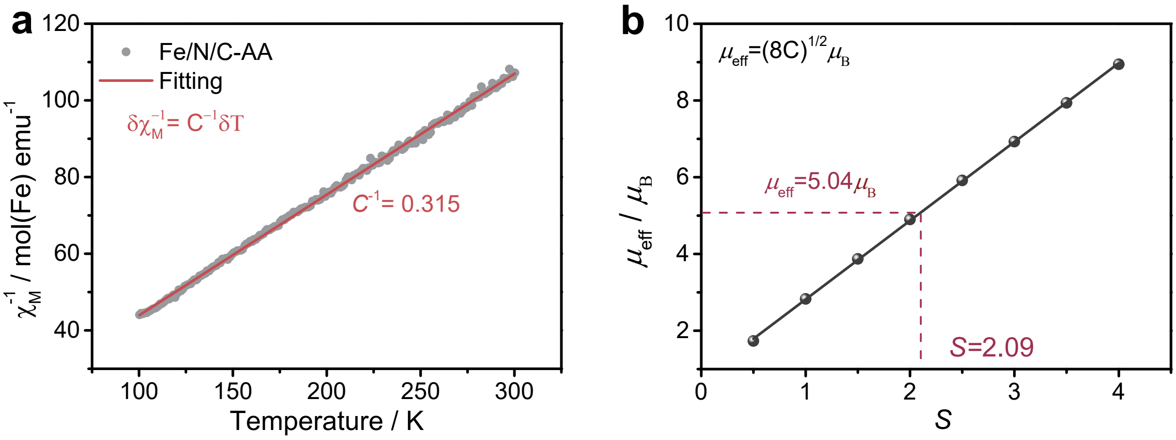

Fig. S9. Determination of spin number of Fe/N/C-AA-2.60wt%. (a) Temperature dependence of the magnetic susceptibility and the calculated Curie constant (C); (b) Calculated average spin state (S) base on theoretical linear relationship between (μ_{eff}) and *S*.

Based on the temperature-dependent magnetization curve, the Curie constant (*C*) was determined using the formula of $\delta\chi^{-1}_{M} = C^{-1}\delta t$. The effective magnetic moment (μ_{eff}) satisfies the formula $\mu_{eff} = (8C)^{1/2}\mu_B$ and the formula $g\sqrt{S(S+1)}\mu_B$, where the g value is approximately 2. Based on the above formula, the spin number of the Fe/N/C-AA-2.60wt% molecule was calculated to be 2.09.

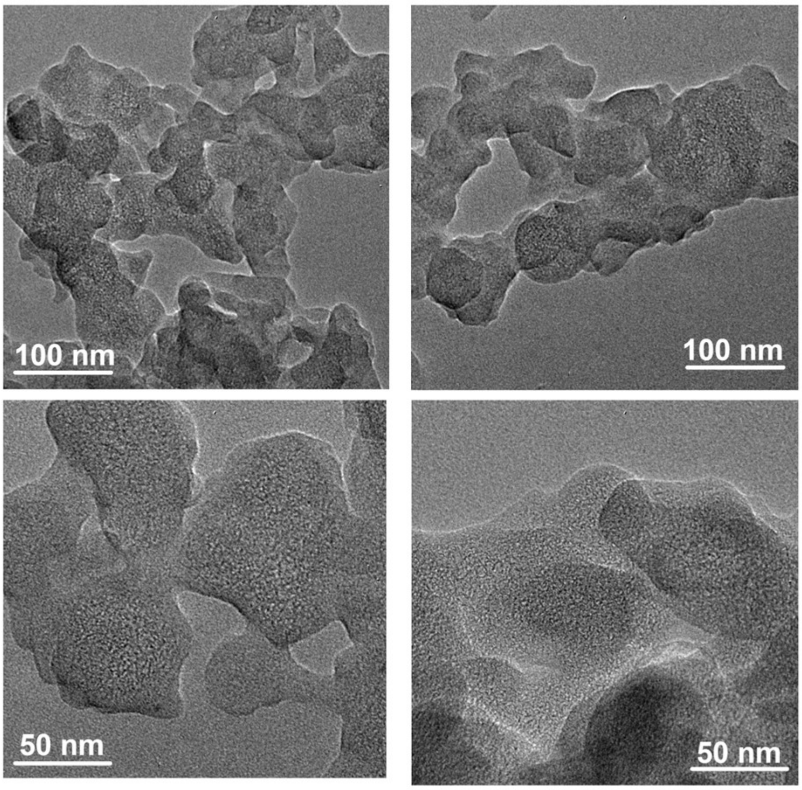

Fig. S10. TEM images of Fe/N/C-0.56wt% at different scales. TEM images at different magnifications detected no Fe particles.

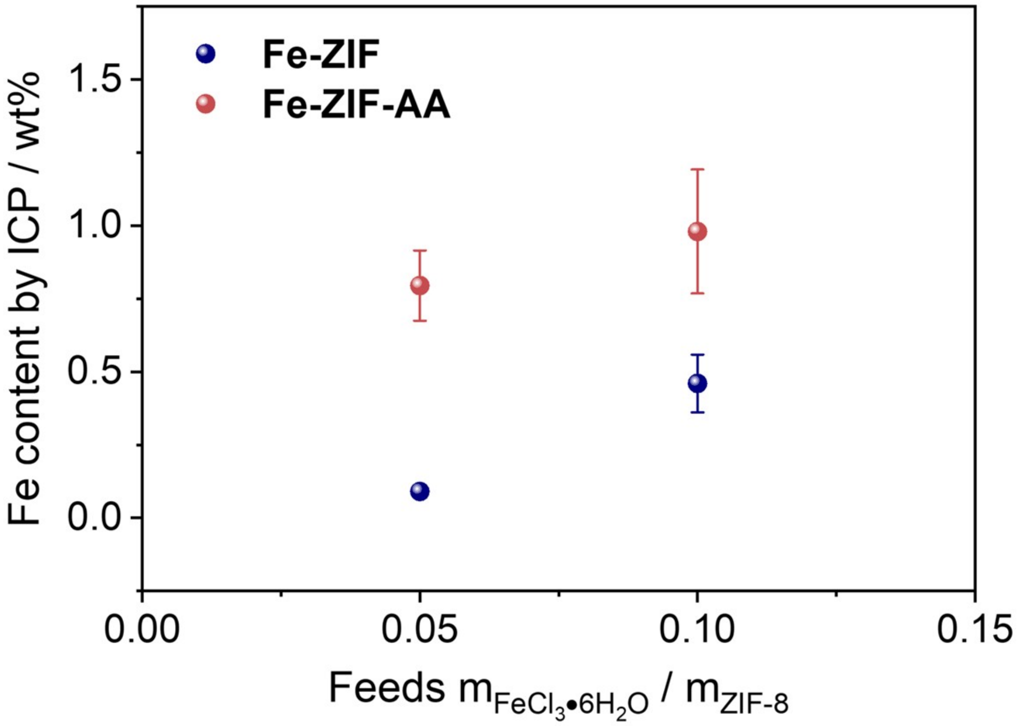

Fig. S11. Fe content in the Fe-ZIF and Fe-ZIF-AA precursors at different feeding ratios.

The Fe content in the Fe-ZIF-AA is higher than that in the Fe-ZIF. This indicates that during doping, AA was oxidized by Fe^{3+} and O_2, producing 2,3-diketogulonic acid and H_2O_2. The possible way that 2,3-diketogulonic acid entered ZIF was to compensate for the excess positive charge that would occur if Zn^{2+} in ZIF was exchanged with Fe^{3+}.

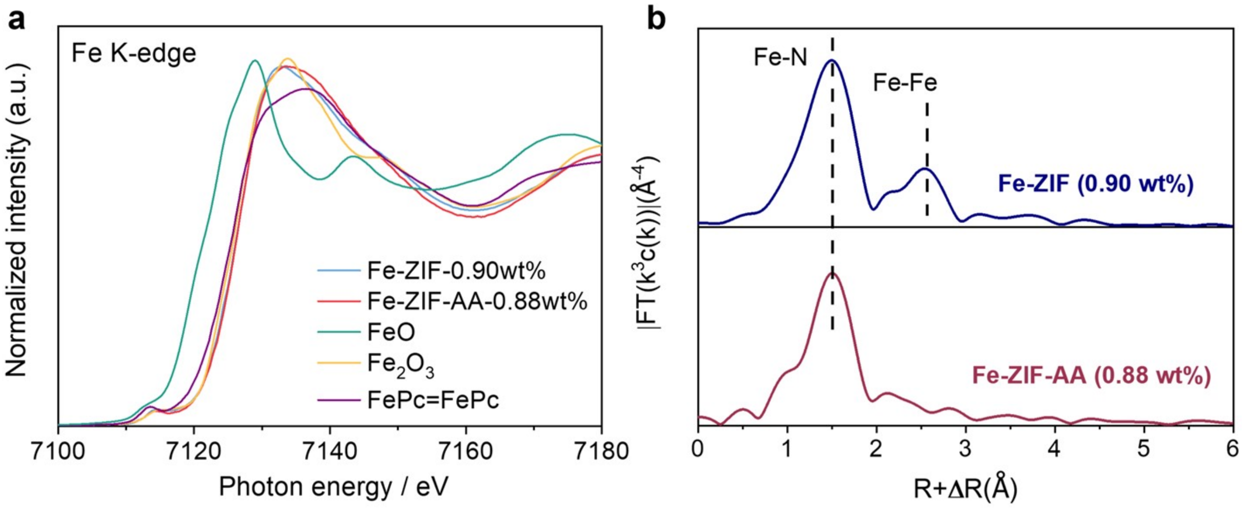

Fig. S12. (a) Fe K-edge XANES and (b) FT-EXAFS analysis of Fe-ZIF and Fe-ZIF-AA precursors. The spectra of the FePc=FePc was extracted from a previous report.[1] This molecule shows the *D*1 state.

Under the condition of the same Fe doping level, the form of Fe in Fe-ZIF and Fe-ZIF-AA precursors differs. In the absence of AA, the doping of Fe sites is non-uniform, leading to the appearance of signals from partial Fe-Fe bonds, possibly originating from Fe (III) oxide/hydroxide. In the presence of AA, Fe still exists in a single-atom state.

The Fe oxidation states in the two Fe-ZIF precursors are slightly higher than that of FePc=FePc. This indicates that the dominant form of Fe in these catalysts is Fe (III). However, while their near-edge spectra exhibit some similarities, they do not fully overlap. This suggests differences in the atomic arrangement of the second coordination shell or beyond, which is reasonable because the atomic arrangement beyond the second coordination layer must differ between FePc=FePc and Fe-ZIF-8.

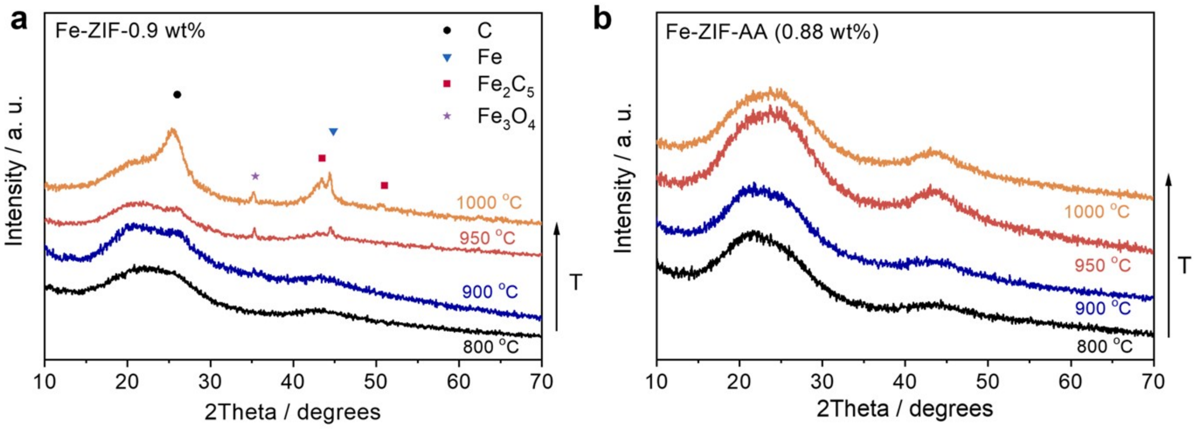

Fig. S13. XRD patterns of (a) Fe-ZIF-0.9wt% and (b) Fe-ZIF-AA-0.88wt% precursors pyrolyzed at different temperature from 800 to 1000 °C.

The XRD patterns of Fe-ZIF-0.9wt% and Fe-ZIF-AA-0.88wt% within the temperature range of 800-1000 °C show that during the pyrolysis of Fe-ZIF-0.9wt%, Fe nanoparticles began to form in the catalyst at 900 °C. In contrast, no detectable formation of Fe nanoparticles was observed for the Fe-ZIF-AA-0.88wt% catalyst over the same temperature range.

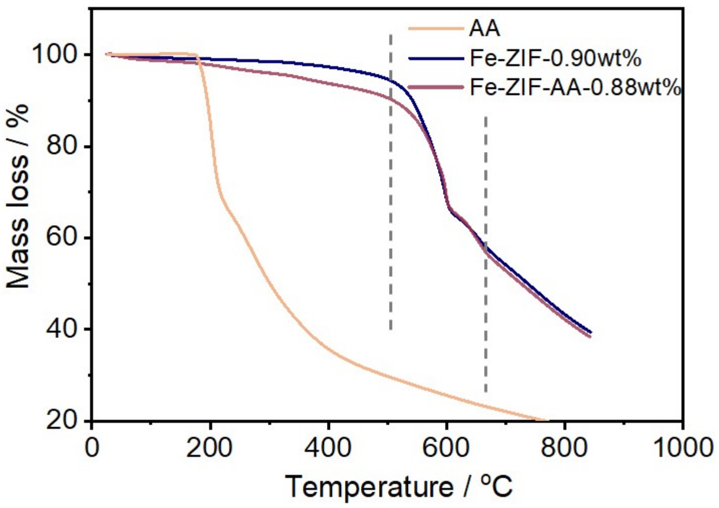

Fig. S14. Thermogravimetric analysis of ZIF, Fe-ZIF and Fe-ZIF-AA.

Thermogravimetric analysis revealed that Fe-ZIF-AA undergoes rapid weight loss in the 200-400°C range, a process associated with the decomposition of 2,3-diketogulonic acid. However, between 500 and 700°C, Fe-ZIF-AA exhibits suppressed weight loss compared to Fe-ZIF. This phenomenon may be attributed to the slower carbothermal reduction process of ZnO, resulting in a more gradual Zn volatilization compared to the AA-free sample. Upon heating above 800°C, ZnO is completely removed, resulting in an expected mass loss trend where Fe-ZIF-AA ultimately shows greater weight loss than its AA-free counterpart.

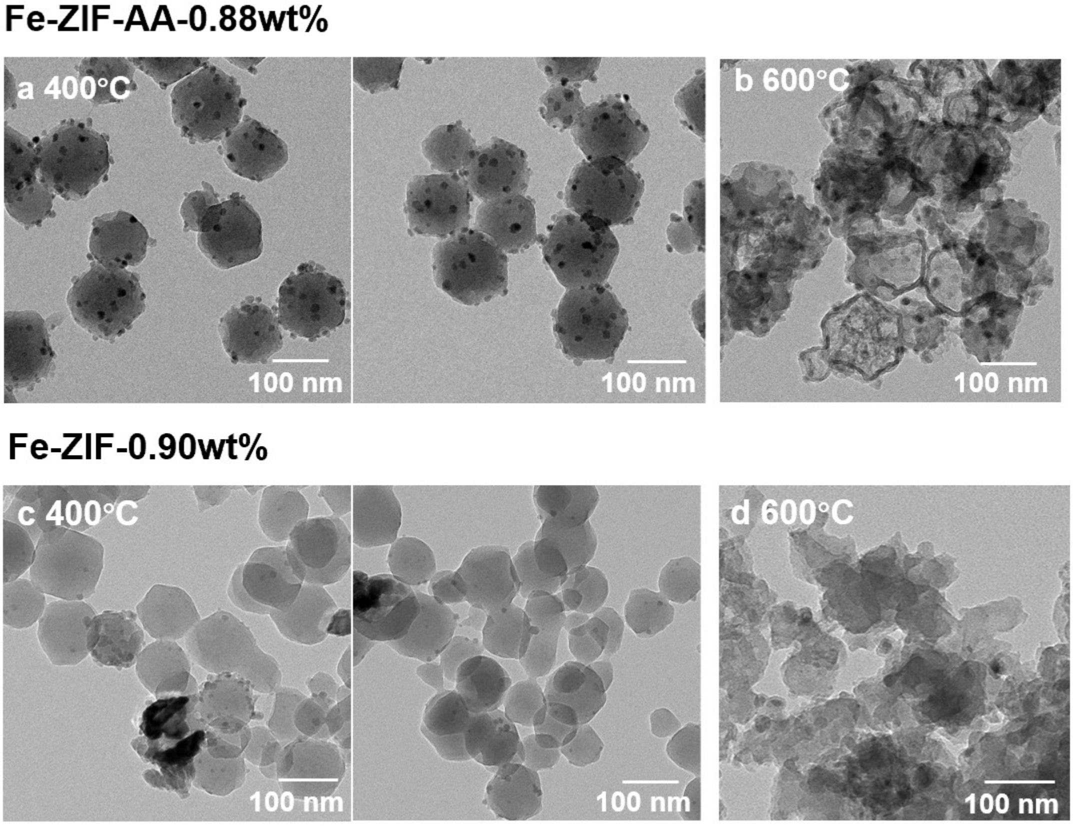

Fig. S15. TEM images of (a, b) Fe-ZIF-AA-0.88wt% after pyrolyzed for 1 hour at 400 and 600 °C. (c, d) Fe-ZIF-0.90wt% after pyrolyzed for 1 hour at 400 and 600 °C.

TEM observed that the AA-modified sample contained a high density of nanoparticles (~10 nm in diameter) at 400°C (Fig. S15a). These nanoparticles were identified as ZnO by XRD analysis (Fig. S16). In comparison, the AA-free sample exhibited only sparsely distributed aggregates of larger ZnO particles (~100 nm in diameter, Fig. S15c). These observations indicate that oxygen species released during AA decomposition facilitated the formation of ZnO nanoparticles. At 600°C, a partial disappearance of ZnO particles was observed. Notably, the AA-containing sample developed numerous etched pore structures (Fig. S15b), whereas no porous features were detected in the AA-free sample (Fig. S15d). The pore formation is likely attributed to the carbothermal reduction of ZnO nanoparticles, which generates substantial amounts of CO gases (or else) that subsequently etch the carbon matrix.

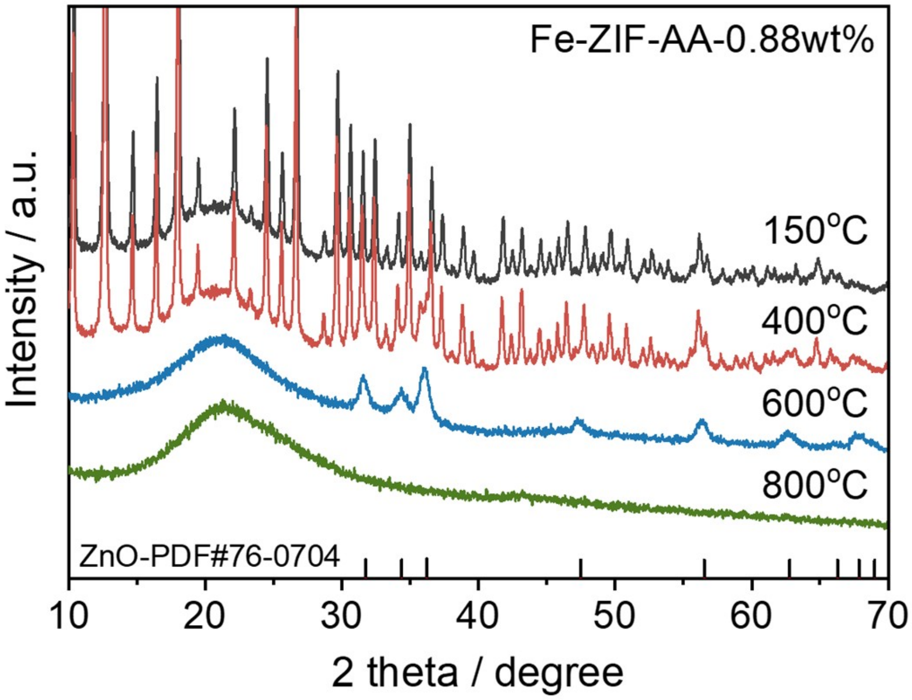

Fig. S16. XRD patterns of Fe-ZIF-AA-0.88wt% precursors pyrolyzed at different temperature for 1 hour from 800 to 1000 °C.

In the temperature range of 150-400°C, the framework structure of ZIF-8 remains observable. However, upon heating to 600°C, the ZIF-8 framework collapses, indicating the decomposition of its primary structure. At this stage, diffraction signals corresponding to ZnO nanoparticles are detected. When the temperature is further elevated to 800°C, the ZnO phase completely disappears.

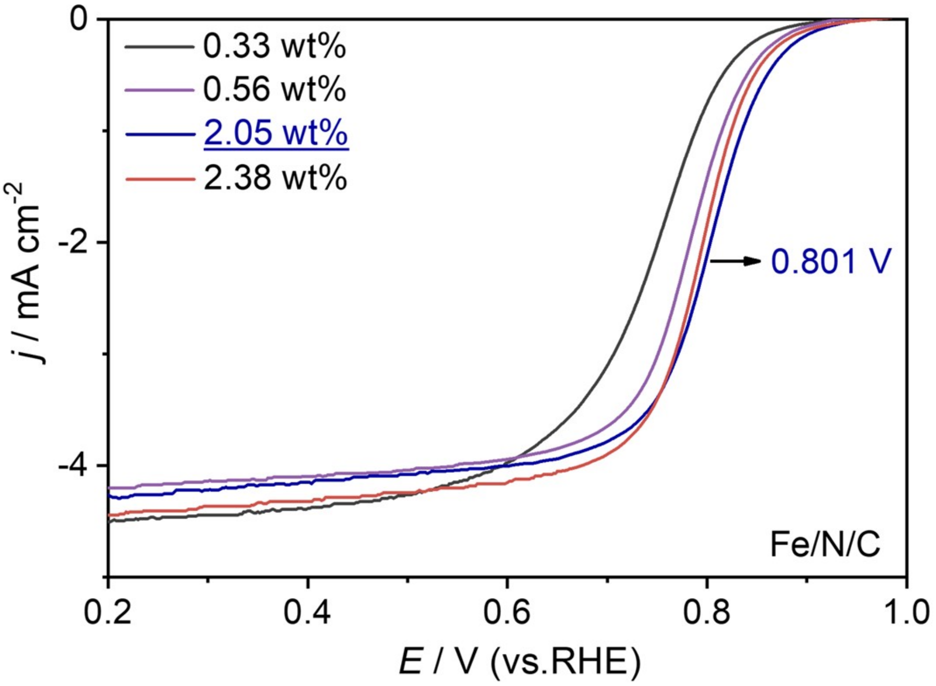

Fig. S17. The ORR activity of Fe/N/C catalysts with different Fe content.

Compared to Fe/N/C at different Fe loadings (0.33 wt.%, 0.56 wt.% and 2.38 wt.%), Fe/N/C- 2.05wt% shows a highest ORR activity with a half-wave potential of 0.801 V_{RHE}.

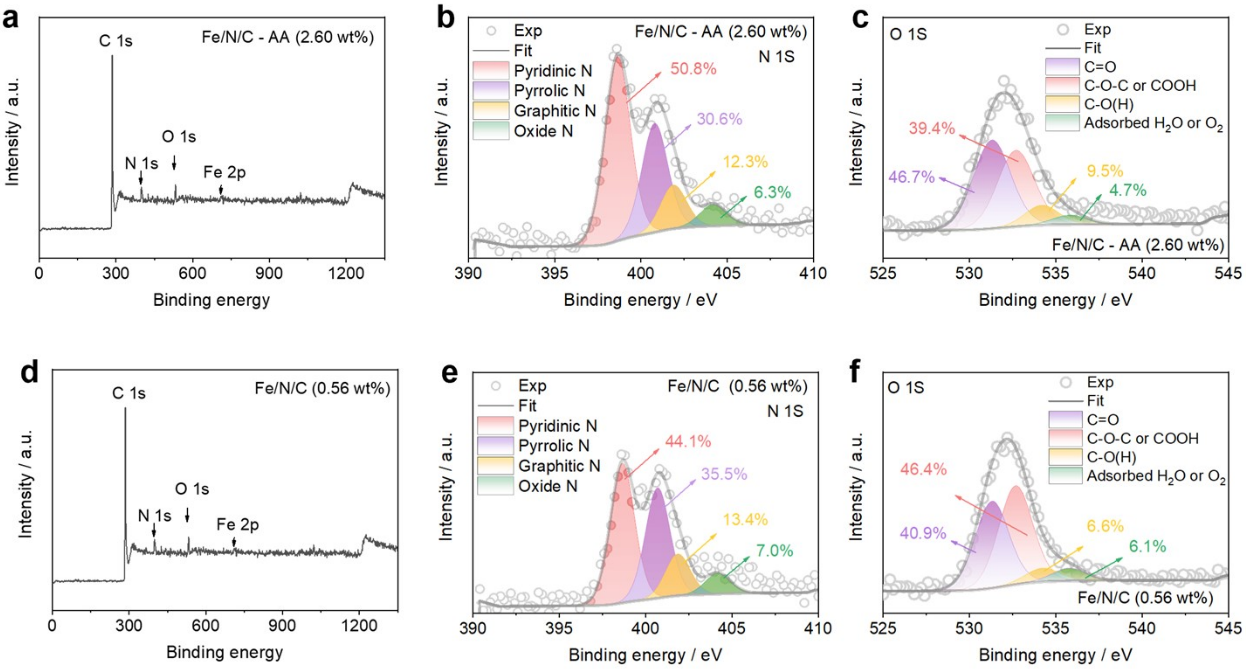

Fig. S18. (a), (d) The XPS full spectrum Fe/N/C-AA-2.60wt% and Fe/N/C-0.56wt%. (b), (e) High-resolution N 1s XPS spectra and the corresponding peak deconvolution. (c), (f) High-resolution O 1s XPS spectra and the corresponding peak deconvolution. The comparative data of the elemental contents in the catalysts and the fitting parameters were shown in Table S4.

Based on the full spectrum data, we compared the surface O content. There is no significant increase in surface O content following the addition of AA. This observation may be attributed to a substantial amount of O has been released in the form of gaseous products such as CO or CO_2, potentially through the reaction of O elements with surface carbon.

In the Fe/N/C-0.56wt% catalyst, the relative contents of pyridine N and pyrrole N are 44.1% and 35.5%, respectively. In contrast, the Fe/N/C-AA-2.60wt% catalyst exhibits relative contents of 50.8% for pyridine N and 30.6% for pyrrole N. This result indicates that the incorporation of AA leads to a higher proportion of pyridine N but less pyrrole N.

The peak fitting data from the O spectrum indicate that, compared to the Fe/N/C-0.56wt% catalyst, the Fe/N/C-AA-2.60 w% catalyst has a higher proportion of C=O components but less C-O-C or C-OOH components.

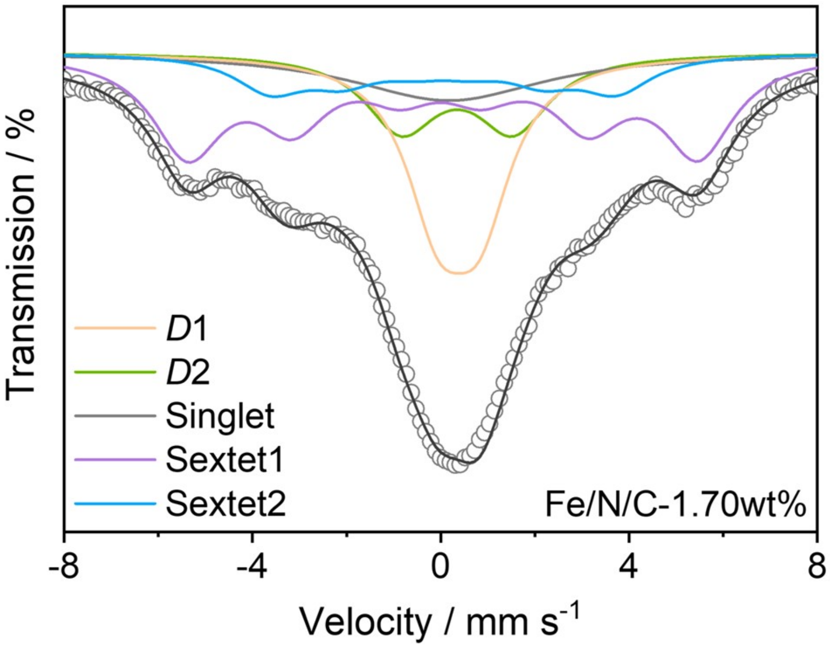

Fig. S19. Low-temperature (77K) Mössbauer spectroscopy of Fe/N/C-1.70wt% catalyst.

The low-temperature Mössbauer spectroscopy of Fe/NC-1.70wt% was fitted with five peaks: *D*1, *D*2, Singlet, Sextet 1, and Sextet 2. At low temperatures, the catalyst exhibited an additional spectral component attributed to α-Fe nanoparticles, which was also observed in the XRD patterns. The emergence of nanoparticle signals at low temperatures that are undetectable at room temperature has also been reported in previous studies[2].

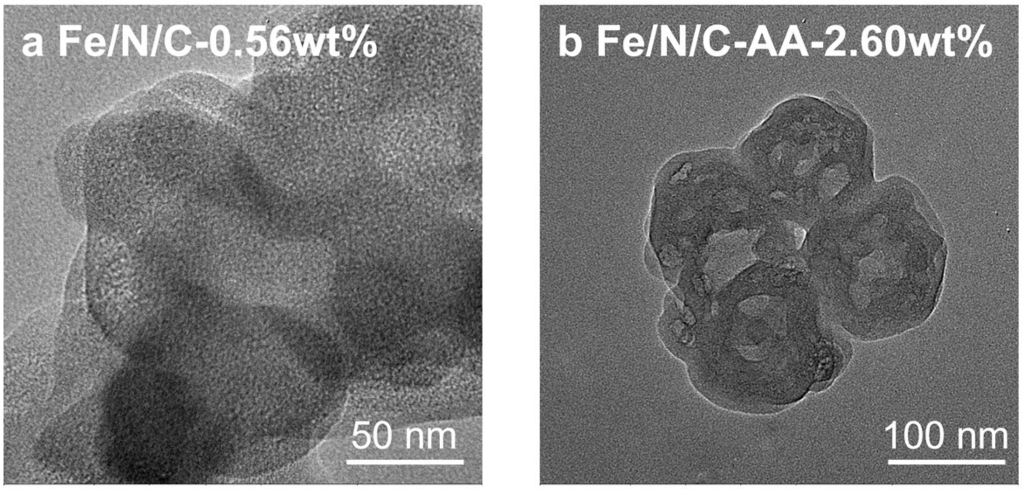

Fig. S20. The TEM images of (a) Fe/N/C-0.56wt% and (b) Fe/N/C-AA-2.60wt%.

TEM images revealed the presence of abundant mesopores in Fe/N/C-AA-2.60wt%, whereas no such mesopores were observed in Fe/N/C-0.56wt%.

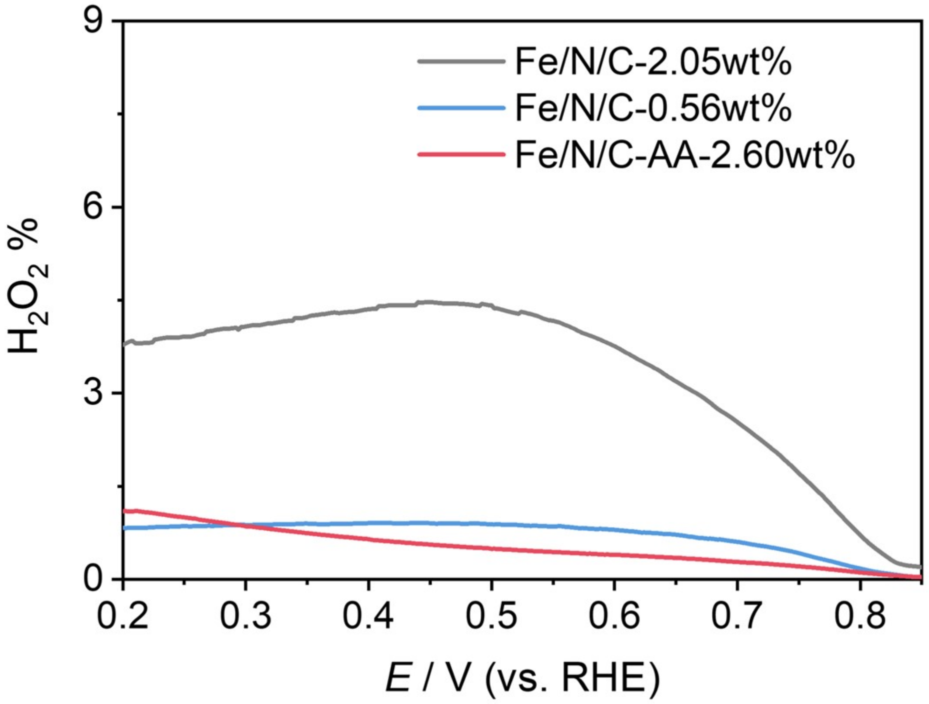

Fig. S21. H_2O_2 yield graphs of Fe/N/C-2.05wt%, Fe/N/C-0.56wt% and Fe/N/C-AA-2.60wt%.

Fe/N/C-2.05wt% showed the highest H_2O_2 yield, followed by Fe/N/C-0.56wt%, while Fe/N/C-AA-2.60wt% had the lowest H_2O_2 yield in the potential range of 0.3～0.85 V_{RHE}.

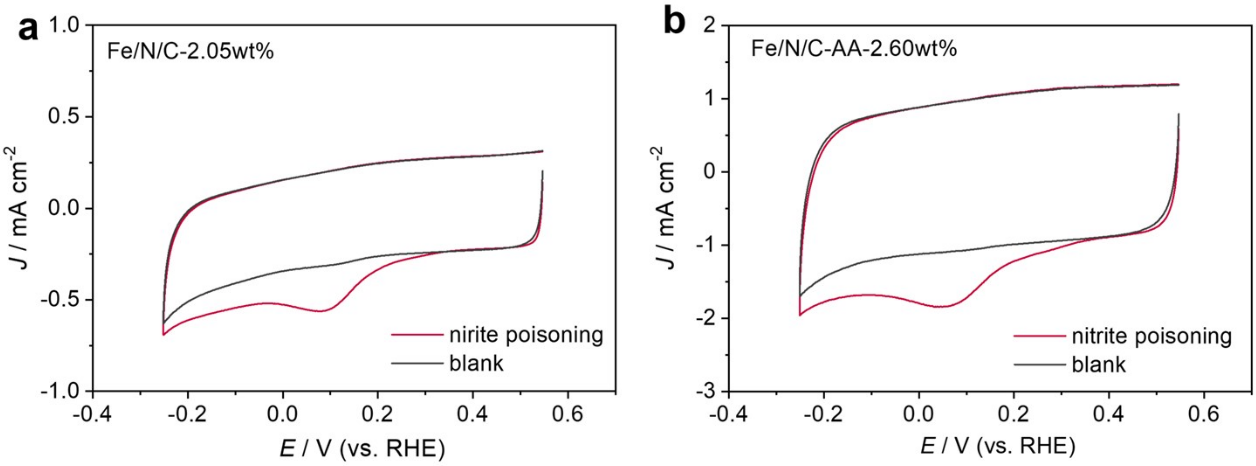

Fig. S22. Nitrite stripping experiments. CV curves of (a) Fe/N/C-2.05wt% and (b) Fe/N/C-AA-2.60wt% catalysts with and without nitrite adsorption for measurement of active site density.

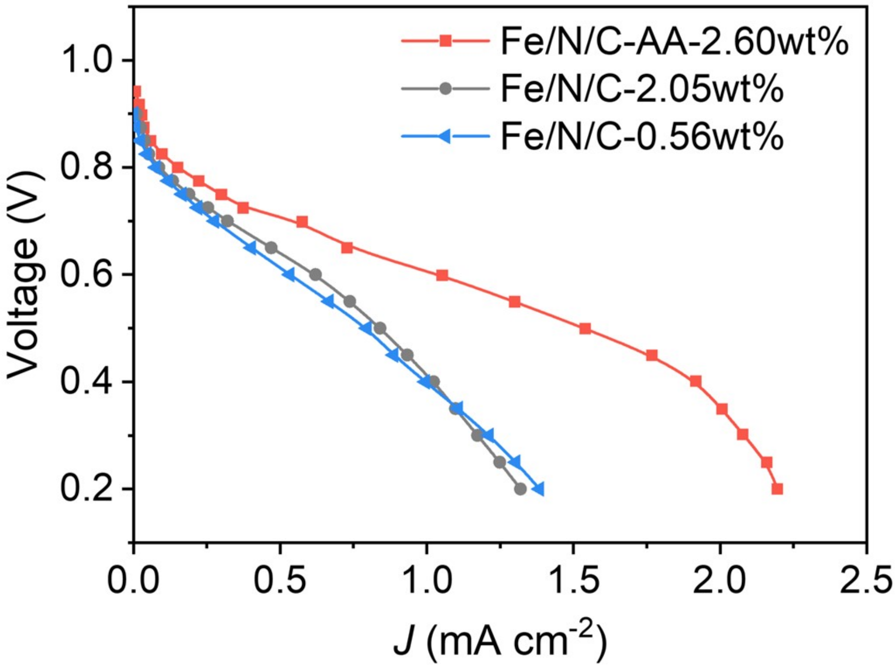

Fig. S23. H_2-air fuel cell polarization curves of the Fe/N/C-2.60wt%, Fe/N/C-2.05wt% and Fe/N/C-0.56wt% cathode catalyst.

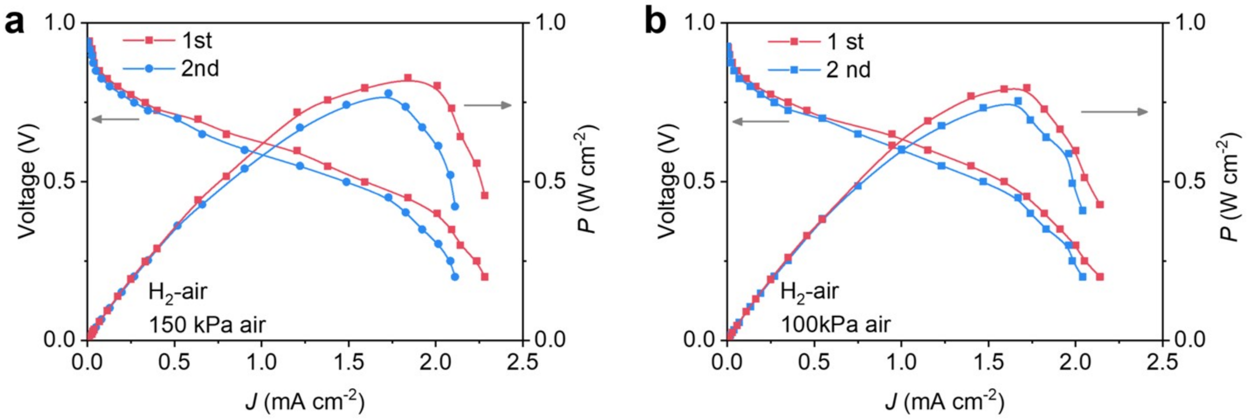

Fig. S24. H_2-air PEMFC polarization performance under different air partial pressures. Two consecutive measurements of H_2-air PEMFC for the Fe/N/C-AA-2.60wt% catalyst. Test conditions: at a cell temperature of 80°C, at 1.7 L min^{-1} of air with 100% RH, at 0.7 L min^{-1} of H_2 with 100% RH, using a Nafion 211 membrane, at a 3.5 mg cm^{-2} of catalyst loading for Fe/N/C-AA, at a Pt loading of 0.4 mg$_{pt}$ cm^{-2} for Pt/C, at an active area of 5.29 cm^2.

In two consecutive measurements, the peak power densities of the Fe/N/C-AA catalyst were recorded as 827 and 778 mW cm^{-2} at 150 kPa air pressure, while under 100 kPa air pressure, the recorded values were 813 and 754 mW cm^{-2}. This indicates that the catalyst activity is rapidly declining during the consecutive tests.

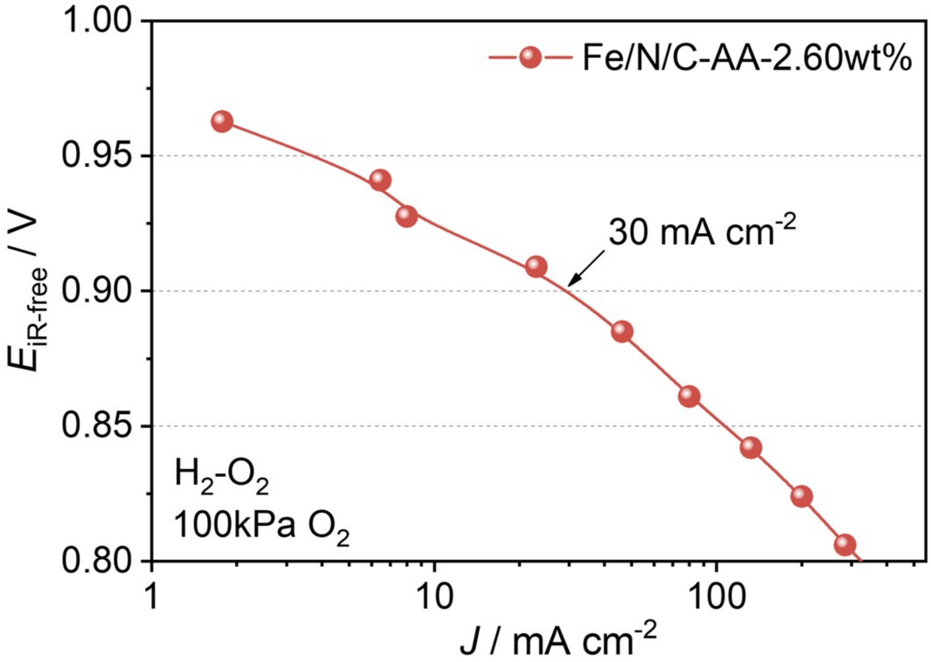

Fig. S25. H_2-O_2 PEMFC polarization curves of Fe/N/C-AA-2.60wt%. Test conditions: at a cell temperature of 80 °C, at 0.35 L min^{-1} of O_2 with 100% RH, at 0.7 L min^{-1} of H_2 with 100% RH, using a Nafion 211 membrane, at a 3.5 mg cm^{-2} of catalyst loading for catalysts, at a Pt loading of 0.4 mg_{pt} cm^{-2} for Pt/C, at an active area of 5.29 cm^2.

Under an O_2 partial pressure of 100 kPa, the current densities at 0.9 V (*i*R-corrected) were 30 mA cm^{-2}, which is lower than several recently reported catalysts (>44 mA cm^{-2}). This result shows that, apart from high intrinsic activity, excellent mass transport characteristics is another critical factor for the enhanced H_2-air performance.

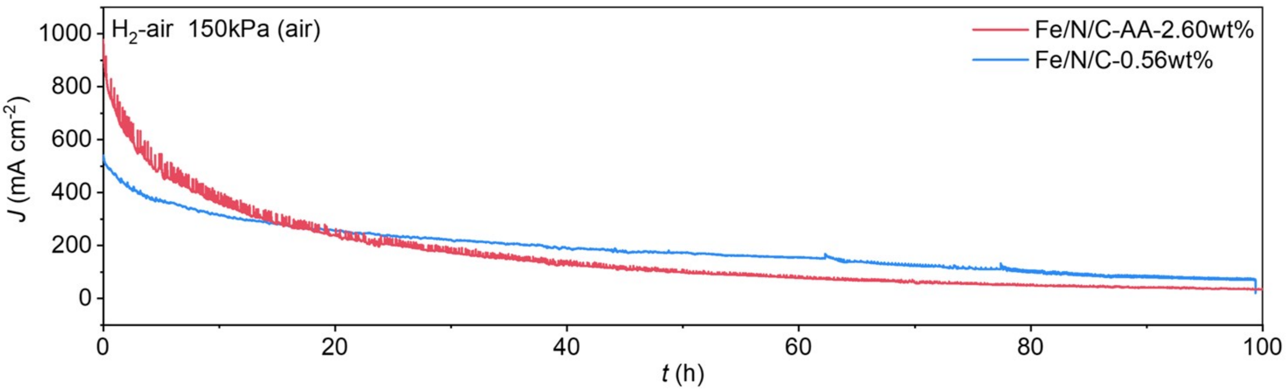

Fig. S26. Fuel cell stability test of Fe/N/C-AA-2.60wt% at a cell voltage of 0.6 V.

During the 100-hour stability test, the Fe/N/C-AA-2.60wt% activity decay reached 97%, while for the Fe/N/C-0.56wt% catalyst with less *D*1 state, the activity decay was 84% in 100 hours. Activity decay appears to be related to the proportion of *D*1 sites.

Table S1. FT-EXAFS fitting parameters for Fe/N/C-AA-2.60wt%.

Sample	Bond	*CN*[a]	*R* (Å)[b]	σ^2(Å^2)[c]	Δ E_0 (eV)[d]	R-factor
Fe/N/C-AA-2.60wt%	Fe-N(O)	5	1.97	0.0125	0.69	0.0028

[a]*CN*: coordination numbers; [b]*R*: bond distance; [c]σ^2: Debye-Waller factors; [d]ΔE_0: the inner potential correction. *R*-factor: goodness of fit. S_0^2 was set to 0.74, according to the experimental EXAFS fit of Fe foil by fixing *CN* as the known crystallographic value.

Table S2a. Results of the fitting of the Mössbauer spectrum of Fe/N/C-AA-2.60wt%, Fe/N/C-0.8wt% and Fe/N/C-1.7wt% acquired at room temperature: relative area (RA, %), isomer shift (*IS*), quadrupole splitting (*QS*), and line width (*LW*) of each component.

^{57}Fe Samples	Assignment	State	*IS* (mm s^{-1})	*QS* (mm s^{-1})	LW (mm s^{-1})	RA (%)
Fe/N/C-AA-2.60wt%	*D*1	*S*=5/2	0.33	0.82	0.59	82
	*D*2	*S*=0 or 1	0.32	2.37	1.18	11
	*D*3	*S*=2	1.12	2.98	0.76	7
Fe/N/C-0.8wt%	*D*1	*S*=5/2	0.33	0.82	0.60	56
	*D*2	*S*=0 or 1	0.33	2.37	1.27	37
	Sextet1	Alpha-Fe*	0	/	0.28	4
	Singlet	Superpara magnetic Fe	0	/	0.98	3
Fe/N/C-1.7wt%	*D*1	*S*=5/2	0.33	0.82	0.59	39
	*D*2	*S*=0 or 1	0.32	2.37	1.17	24
	Singlet	Superpara magnetic Fe	-0.09	/	0.31	17
	Sextet2	Iron carbide	0.03	/	0.36	20

* Due to the lower scanning speed, the full signal of the six peaks was not displayed; instead, only the signal of four peaks was shown.

Table S2b. Results of the fitting of the Mössbauer spectrum of Fe/N/C-AA-2.60wt% and Fe/N/C-1.7wt% acquired at 77K: relative area (RA, %), isomer shift (*IS*), quadrupole splitting (*QS*), and line width (*LW*) of each component.

^{57}Fe Samples	Assignment	State	*IS* (mm s^{-1})	*QS* (mm s^{-1})	LW (mm s^{-1})	RA (%)
Fe/N/C-AA-2.60wt%	*D*1	*S*=5/2	0.38	0.88	1.66	82
	*D*2	*S*=0 or 1	0.35	2.37	1.70	11
	*D*3	*S*=2	1.12	2.98	1.34	7
Fe/N/C-1.70wt%	*D*1	*S*=5/2	0.38	0.88	1.66	24
	*D*2	*S*=0 or 1	0.35	2.37	1.88	14
	Singlet	Superparamagnetic Fe	0.17	/	5.00	12
	Sextet1	α-Fe	0.01	0.05	1.83	37
	Sextet2	Iron carbide	0.05	0.01	1.84	13

Table S3. Summary of the content of *D*1 state in recently reported Fe-N-Cs.

Samples	*D*1 / %	Fe / wt%	$D1_{\mathrm{Fe}}$ / wt%	Ref.
Fe/N/C-AA-2.60wt%	**82.0**	**2.60**	**2.13**	**This work**
FeNC-CVD-750	89.0	2.00	1.78	[3]
F-FeNC-2	78.0	1.68	1.31	[4]
FeNC-Pd_{NC}	70.3	0.36	0.25	[5]
P(AA-MA)-Fe-N	70.0	1.10	0.77	[6]
Fe-AC	65.0	1.75	1.14	[7]
$Fe_{0.5}$	64.1	1.50	0.96	
FeNC-1100	59.0	0.62	0.36	[9]
Fe-AC-CVD	53.0	1.69	0.89	[7]
PANI-MeI	50.5	1.17	0.59	[10]

Table S4. Summary of XPS fitting parameters and element contents for Fe/N/C-AA-2.60wt% and Fe/N/C-0.56wt% catalysts.

Full spectrum

Atomic content (%)	**Fe/N/C-AA-2.60wt%**	**Fe/N/C-0.56wt%**
C 1s	89.8	89.3
O 1s	4.57	4.93
N 1s	5.37	5.74
Fe 2p	0.26	0.03

N 1s

Fe/N/C-AA-2.60wt%	Binding energy / eV	FWHM	Area	Atomic / %
Pyridinic N	398.7	1.83	1023	50.8
Pyrrolic N	400.8	1.86	615	30.6
Graphitic N	401.9	1.86	247	12.3
Oxide N	404.2	1.93	127	6.3
Fe/N/C-0.56wt%	Binding energy / eV	FWHM	Area	Atomic / %
Pyridinic N	398.7	1.73	733	44.1
Pyrrolic N	400.7	1.76	591	35.5
Graphitic N	401.9	1.76	224	13.4
Oxide N	404.2	1.83	117	7.0

O 1s

Fe/N/C-AA-2.60wt%	Binding energy / eV	FWHM	Area	Atomic / %
C=O	531.3	2.66	1206	46.4
C-O-C or COOH	532.7	2.62	1022	39.4
C-O(H)	534.2	2.41	247	9.5
Adsorbed H_2O or O_2	535.8	2.49	122	4.7
Fe/N/C-0.56wt%	Binding energy / eV	FWHM	Area	Atomic / %
C=O	531.3	2.41	1256	40.9
C-O-C or COOH	532.7	2.41	1426	46.4
C-O(H)	534.3	2.45	202	6.6
Adsorbed H_2O or O_2	535.8	2.41	186	6.1

Table S5. Summary of ASD and site TOF for Fe/N/C-2.05wt% and Fe/N/C-AA-2.60wt%.

Sample	Fe/N/C-2.05wt%	Fe/N/C-AA-2.60wt%
ASD (μmol sites g^{-1})	50	162
TOF (mA μmol^{-1})	27	34

Table S6. Performance comparison of H_2-air PEMFC employing non-precious metal catalyst as the cathode catalyst.

Catalyst	Operation temperature / °C	Catalyst loading / mg cm^{-2}	P_{Back} / bar	$J_{0.8\mathrm{V}}$ / mA cm^{-2}	$P_{\max}$ / mW cm^{-2}	Area / cm^2	Year	Ref.
Fe/N/C-AA-2.60wt%	**80**	**3.5**	**1**	**174/127***	**827/778***	**5.29**	**2024**	**This work**
Fe/N/C-AA-2.60wt%	**80**	**3.5**	**0.5**	**164/132***	**796/754***	**5.29**	**2024**	
Fe-N-C-FG	80	4.5	1	191	725	5	2023	[11]
Fe_g-NC	80	3.5	1	140	711	4.41	2022	[12]
Fe-MOF	94	4.0	1	194	610	5	2019	[13]
Fe/N/C(4mlm)-OAc	80	3.0	1	72	467	1.21	2021	[14]
TPI@Z8(SiO_2)	80	2.0	1	105	420	5	2019	[15]
(CM+PANI)-Fe-C	80	4.0	1	99	420	5	2017	[16]
MesoS/MicroC-FeNC	80	2.7	1	130	400	5	2022	[17]

*The two data correspond to the results of two consecutive measurements of a same MEA. A 15-minute interval was introduced between consecutive polarization curve measurements to ensure a stable OCP value prior to the second measurement. The observed difference between the two measurements is attributed to the rapid decay of the *D*1 state.

Reference:

1. K. M. Zhao, D. X. Wu, W. K. Wu, J. B. Nie, F. S. Geng, G. Li, H. Y. Shi, S. C. Huang, H. Huang, J. Zhang, Z. Y. Zhou, Y. C. Wang and S. G. Sun, *Nat. Catal.*, 2025, DOI: 10.1038/s41929-025-01324-7.
2. L. M. Ni, C. Gallenkamp, S. Paul, M. Kübler, P. Theis, S. Chabbra, K. Hofmann, E. Bill, A. Schnegg, B. Albert, V. Krewald and U. I. Kramm, *Adv. Energy Sustain. Res.*, 2021, **2**, 2000064.
3. L. Jiao, J. Li, L. L. Richard, Q. Sun, T. Stracensky, E. Liu, M. T. Sougrati, Z. Zhao, F. Yang, S. Zhong, H. Xu, S. Mukerjee, Y. Huang, D. A. Cullen, J. H. Park, M. Ferrandon, D. J. Myers, F. Jaouen and Q. Jia, *Nat. Mater.*, 2021, **20**, 1385-1391.
4. X. F. Tao, R. H. Lu, L. M. Ni, V. Gridin, S. H. Al-Hilfi, Z. J. Qiu, Y. Zhao, U. I. Kramm, Y. Z. Zhou and K. Müllen, *Mater. Horiz.*, 2022, **9**, 417-424.
5. X. Q. Wei, S. J. Song, W. Y. Song, Y. T. Wen, W. Q. Xu, Y. F. Chen, Z. C. Wu, Y. Qin, L. Jiao, Y. Wu, M. Sha, J. J. Huang, X. L. Cai, L. R. Zheng, L. Y. Hu, W. L. Gu, M. Eguchi, T. Asahi, Y. Yamauchi and C. Z. Zhu, *Chem. Sci.*, 2022, **13**, 13574-13581.
6. Z. P. Miao, X. M. Wang, Z. L. Zhao, W. B. Zuo, S. Q. Chen, Z. Q. Li, Y. H. He, J. S. Liang, F. Ma, H. L. Wang, G. Lu, Y. H. Huang, G. Wu and Q. Li, *Adv. Mater.*, 2021, **33**, 2006613.
7. S. W. Liu, C. Z. Li, M. J. Zachman, Y. C. Zeng, H. R. Yu, B. Y. Li, M. Y. Wang, J. Braaten, J. W. Liu, H. M. Meyer, M. Lucero, A. J. Kropf, E. E. Alp, Q. Gong, Q. R. Shi, Z. X. Feng, H. Xu, G. F. Wang, D. J. Myers, J. Xie, D. A. Cullen, S. Litster and G. Wu, *Nat. Energy*, 2022, **7**, 652-663.
8. J. K. Li, M. T. Sougrati, A. Zitolo, J. M. Ablett, I. C. Oguz, T. Mineva, I. Matanovic, P. Atanassov, Y. Huang, I. Zenyuk, A. Di Cicco, K. Kumar, L. Dubau, F. Maillard, G. Drazic and F. Jaouen, *Nat. Catal.*, 2021, **4**, 10–19.
9. D. S. Xia, X. Tang, S. Dai, R. L. Ge, A. Rykov, J. H. Wang, T. H. Huang, K. W. Wang, Y. P. Wei, K. Zhang, J. Li, L. Gan and F. Y. Kang, *Adv. Mater.*, 2023, **35**, 2204474.
10. N. D. Leonard, S. Wagner, F. Luo, J. Steinberg, W. Ju, N. Weidler, H. Wang, U. I. Kramm and P. Strasser, *ACS Catal.*, 2018, **8**, 1640-1647.
11. Y. C. Zeng, C. Z. Li, B. Y. Li, J. S. Liang, M. J. Zachman, D. A. Cullen, R. P. Hermann, E. E. Alp, B. Lavina, S. Karakalos, M. Lucero, B. Z. Zhang, M. Y. Wang, Z. X. Feng, G. F. Wang, J. Xie, D. J. Myers, J. P. Dodelet and G. Wu, *Nat. Catal.*, 2023, **6**, 1215-1227.
12. S. H. Yin, S. L. Yang, G. Li, G. Li, B. W. Zhang, C. T. Wang, M. S. Chen, H. G. Liao, J. Yang, Y. X. Jiang and S. G. Sun, *Energy Environ. Sci.*, 2022, **15**, 3033-3040.
13. A. Uddin, L. Dunsmore, H. G. Zhang, L. M. Hu, G. Wu and S. Litster, *ACS Appl. Mater. Interfaces*, 2020, **12**, 2216-2224.
14. Y. Y. Li, P. Y. Zhang, L. Y. Wan, Y. P. Zheng, X. M. Qu, H. K. Zhang, Y. S. Wang, K. Zaghib, J. Y. Yuan, S. H. Sun, Y. C. Wang, Z. Y. Zhou and S. G. Sun, *Adv. Funct. Mater.*, 2021, **31**, 7.
15. X. Wan, X. F. Liu, Y. C. Li, R. H. Yu, L. R. Zheng, W. S. Yan, H. Wang, M. Xu and J. L. Shui, *Nat. Catal.*, 2019, **2**, 259-268.
16. H. T. Chung, D. A. Cullen, D. Higgins, B. T. Sneed, E. F. Holby, K. L. More and P. Zelenay, *Science*, 2017, **357**, 479-483.
17. L. Chen, X. Wan, X. N. Zhao, W. W. Li, X. F. Liu, L. R. Zheng, Q. T. Liu, R. H. Yu and J. L. Shui, *J. Mater. Chem. A*, 2022, **10**, 7764-7772.